



# Numerical simulation and experimental study of laser cladding Ni-based powder on 45# steel surface

Haiyang Long<sup>1,2</sup> · Tiankai Li<sup>1</sup> · Zhen Dong<sup>1</sup> · Yongliang Gui<sup>2</sup> · Changming Qiu<sup>1</sup> · Mingming Wang<sup>1</sup> · Dongdong Li<sup>1</sup>

Received: 23 December 2022 / Accepted: 1 October 2023 / Published online: 14 October 2023  
© The Author(s), under exclusive licence to Springer-Verlag London Ltd., part of Springer Nature 2023

## Abstract

The cladding process is the key factor in determining the quality and efficiency of cladding, and in-depth study of process characteristics has practical importance for the application of this technology in industries. The temperature and stress fields under different process parameters were studied to determine the optimal process parameters. The optimal process parameters were chosen according to the morphology of the cladding layer. On this basis, the cooling rate, temperature gradient and solidification rate of the coating in different depth directions were calculated, and the formation mechanism of the cladding layer morphology was revealed. In addition, the microstructure and hardness of the coating were characterised and tested, respectively. Results show that the microstructure of the coating is mainly composed of  $\gamma(\text{Ni})$ ,  $\text{FeNi}_3$ ,  $\text{M}$  ( $\text{M} = \text{Fe}, \text{Ni}, \text{Cr}$ )<sub>23</sub> $\text{C}_6$ ,  $\text{M}_7\text{C}_3$ , and  $\text{CrB}$ . The hardness of the optimised coating is 600 HV<sub>0.2</sub>, and the hardness of 45# steel is improved. This work has a certain guiding significance for engineering applications to repair 45# steel parts through numerical simulation and experimental combinations.

**Keywords** Laser cladding · Numerical simulation · Microstructure · Formation mechanism

## 1 Introduction

The 45# steel is a high-quality carbon structural steel with many advantages, such as low cost, high strength and plasticity. Therefore, it has been applied to various key parts, such as machine tool spindles, rack shafts and gears [1, 2]. However, the complex and poor service conditions for the parts mentioned above result in significantly lower surface performance and increased maintenance costs. Manufacturing wear-resistant and corrosion-resistant coatings is an effective method to strengthen the surface performance of engineering parts in severe operating conditions.

Laser cladding technology is a new repair technology developed on the basis of laser reconstruction. This technology has a smaller grain size, more compact structure and lower dilution rate than traditional chemical heat treatment. Therefore, this technology has been widely utilised for surface strengthening [3–6]. However, the sharp rise and fall of temperature results in complex residual stress. This condition will immediately lead to crack defects, which shortens the service life of parts [7–9]. Therefore, the residual stress needs to be reduced.

Laser cladding technology is a surface modification technology that involves complex thermodynamics. The advent of simulation software has facilitated the wide use of the finite element method in

---

✉ Haiyang Long  
lhy@ncst.edu.cn

Tiankai Li  
18833790174@163.com

Zhen Dong  
dz15612873917@163.com

Yongliang Gui  
gyl@ncst.edu.cn

Changming Qiu  
qcm@ncst.edu.cn

Mingming Wang  
wangmingming@ncst.edu.cn

Dongdong Li  
lidongdong@ncst.edu.cn

<sup>1</sup> College of Mechanical Engineering, North China University of Science and Technology, 21 Bohai Road, Caofeidian Xincheng, Tangshan 063210, China

<sup>2</sup> College of Metallurgy and Energy, North China University of Science and Technology, 21 Bohai Road, Caofeidian Xincheng, Tangshan 063210, China

characterising laser cladding processes. Yong et al. [10] prepared a visual inspection of the Ni60 alloy coating molten pool, extracted the size, area, width, length and other information of the molten pool and used ANSYS to simulate the temperature field. The results show that the model predicts the area of the molten pool, width and length with accuracies of 9% and ~20%. Gao et al. [11] built a numerical model of Fe-based coatings and realised the temperature field distribution law of different process parameter combinations. The solidification and cooling rates of the solid–liquid interface are analysed by calculation and experiment. Zhang et al. [12] used ANSYS to simulate the temperature and stress fields of single-track cladding of an Fe–Mn–Si–Cr–Ni shape memory alloy coating. The simulation results show that the shape of the molten pool of the circular spot single-track laser cladding is half a spoon. The residual stress analysis of the coating shows that the longitudinal residual stress of the coating is the largest with a value of approximately 300 MPa. The transverse residual stress is the smallest. Vundru et al. [13] adopted ABAQUS software to establish a thermodynamic coupling model, simulate the evolution of residual stress along the cross section of the coating and determine the optimal process conditions corresponding to the reduction in tensile residual stress.

In summary, numerical simulation is an effective way to investigate the distribution of the temperature and stress fields of laser cladding. However, research on the distribution of the temperature and stress fields in laser cladding under different laser processing parameters and their influence on forming quality is relatively few, and studies on experiments and digital simulation systems are also rare. Therefore, this work explores the effect of process parameters on coating quality. Single-pass laser cladding is established by the MODELCHANGE function of ABAQUS software and the USDFLD subroutine edited by FORTRAN. Temperature and residual stress with different process parameters are simulated, and the optimal process parameters are selected according to the morphology of the coating. In the case of the optimal process parameters, the distribution characteristics of the temperature and stress fields are explored first. Then, the microstructure and microhardness are characterised. The formation mechanism of the coating structure is revealed on the basis of the simulation and experimental results.

## 2 Experimental methods

The substrate and cladding materials used in this experiment were 45# steel and Ni60PTA powder, respectively. The compositions of the two materials are shown in Table 1. A TSR-2000–1 fibre laser was used as the equipment. The phase analysis of the coating was

performed by X-ray diffraction (XRD) and Cu-K $\alpha$  radiation at operating voltages of 60 kV and 300 mA. Before the test, the test piece was cut into the required size, polished with sandpaper and then ultrasonically cleaned with acetone and anhydrous ethanol. The metallographic structure was observed by optical microscopy (OM) and scanning electron microscopy (SEM) equipped with energy dispersive spectroscopy (EDS). The laser radius was measured by CCD imaging. A Vickers hardness tester with a load of 200 g was utilised to acquire the hardness of the longitudinal section of the coating at room temperature, with an interval of 0.2 mm from the top surface of the coating until the heat-affected zone of the substrate was exceeded. Three groups of hardness were measured and then averaged to avoid errors.

## 3 Numerical modelling

### 3.1 Governing equation

The whole cladding process is understood as a nonlinear heat conduction process, which is analysed by the continuous discrete method. The following equation can be used to describe the heat conduction law [14, 15]:

$$\frac{\partial T}{\partial t} = \frac{\lambda}{\rho c} \left( \frac{\partial^2 T}{\partial x^2} + \frac{\partial^2 T}{\partial y^2} + \frac{\partial^2 T}{\partial z^2} \right) + Q \quad (1)$$

where  $\rho$  is density,  $c$  is temperature-dependent specific heat capacity,  $T$  is the temperature,  $Q$  is internal heat source heat and  $\lambda$  is temperature-dependent thermal conductivity.

### 3.2 Initial and boundary conditions

The initial condition is that the temperature of the object at the beginning must be given for unsteady heat conduction. The assumption is that the initial temperature of the workpiece is the ambient temperature [16]:

$$T(x, y, z, t)|_{t=0} = T_0 \quad (2)$$

where  $T_0$  is the initial temperature,  $T_0 = 25$  °C.

The sum of the heat dissipated by the material due to thermal convection and radiation and the heat lost by the heat conduction of the material is equal to the laser heat absorbed by the powder material. The boundary conditions are as follows:

$$\lambda \frac{\partial T}{\partial n} = q_s - q_{\text{convection}} - q_{\text{radiation}} \quad (3)$$

**Table 1** Chemical composition of 45# steel and Ni60PTA (wt%)

Materials	C	Si	Mn	P	S	Cr	Ni	Fe	B	Mo
45# steel	0.42	0.2	0.7	0.025	0.024	0.23	0.14	Bal	-	-
Ni60PTA	1.21	5.83	-	-	-	20.17	Bal	4.13	2.79	0.21

Thermal convection and thermal radiation can be expressed as

$$q_{convection} = h(T_s - T_\infty) \tag{4}$$

$$q_{radiation} = \sigma \epsilon (T_s^4 - T_\infty^4) \tag{5}$$

where  $\epsilon$  is the thermal radiation coefficient,  $\sigma$  is the Stefan Boltzmann constant ( $5.67 \times 10^8 \text{ W/m}^2 \text{ K}^4$ ),  $h$  is the convection heat transfer coefficient,  $T_s$  is the surface temperature,  $T_\infty$  is the external ambient temperature and  $q_s$  is the input heat.

### 3.3 Heat source selection

In previous studies, Gaussian heat sources were mainly used for simulation. To realise the generation of a heat source, the moving heat source subroutine DFLUX [17] is written in FORTRAN and is then used with the model for heat transfer calculation [18]:

$$q = \frac{2AP}{\pi R^2} \exp\left(-\frac{2[(x-x_0)^2 + (z-z_0-vt)^2]}{R^2}\right) \tag{6}$$

where  $P$  is the laser power,  $A$  is the absorption efficiency,  $t$  is the time,  $v$  is the scanning speed and  $R$  is the radius of the experimentally measured laser beam.

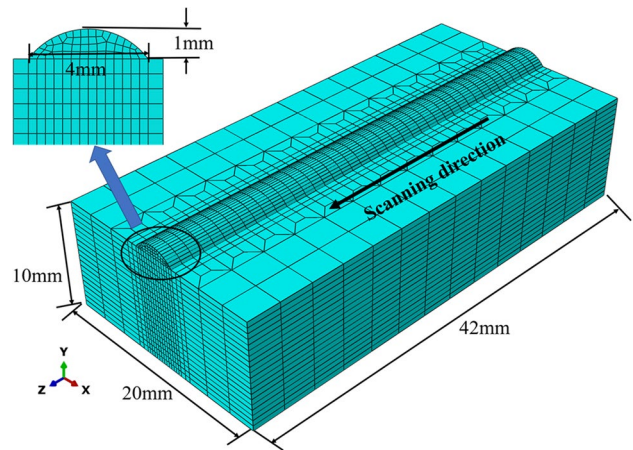


Fig. 2 Grid division model

### 3.4 Assumptions and thermophysical parameters

The process of laser cladding is relatively complex. The finite element model of laser cladding needs to be reasonably simplified and assumed to reduce the calculation amount and improve the calculation efficiency [19].

- (1) The isotropic continuum can satisfy the calculation accuracy, and the calculation amount is small. So the cladding alloy powder is simplified into an isotropic continuum [20, 21].

Fig. 1 Thermal physical parameters of materials: **a** 45# steel thermal properties, **b** 45# steel mechanical properties, **c** Ni60PTA thermal properties and **d** Ni60PTA mechanical properties

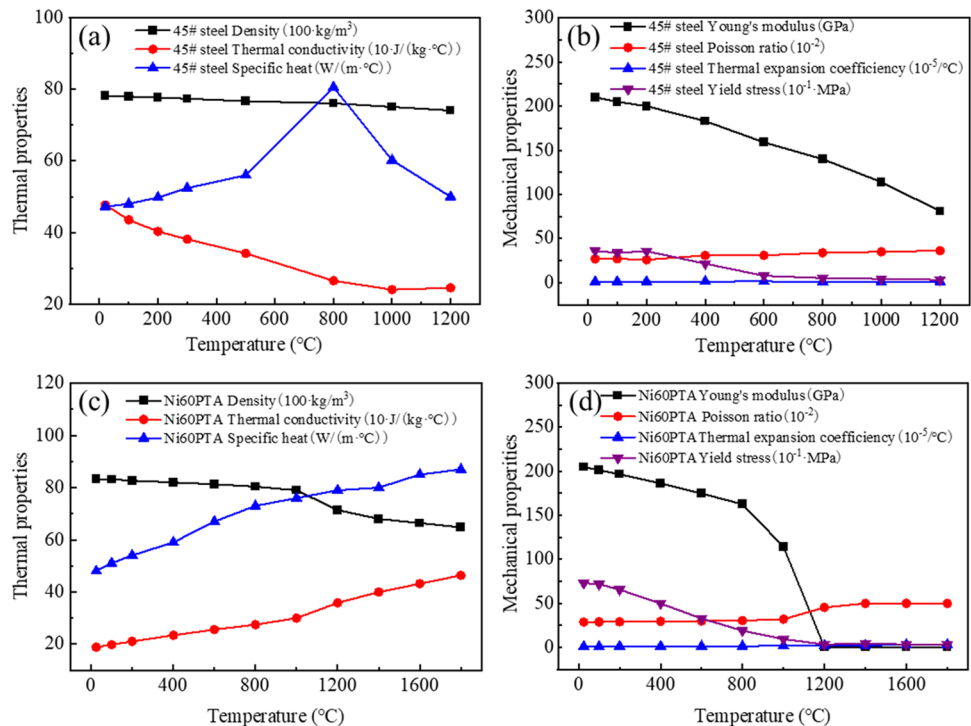


**Table 2** Simulation scheme

Laser power (W)	Scanning speed (mm/s)	Laser beam diameter (mm)
1400	3	4
1400	4	4
1400	5	4
1500	3	4
1500	4	4
1500	5	4
1600	3	4
1600	4	4
1600	5	4

- (2) The distribution of cladding material is uniform and smooth. The absorption rate of the laser does not vary with temperature.
- (3) In this paper, the temperature field and stress field are mainly analysed, and the morphology of the molten pool is not much explored. Therefore, the Marangoni effect is not considered [22, 23].

(4) The heat conduction between the substrate and the test bench is disregarded.

The thermophysical parameters of metal materials have an important effect on the accuracy of finite element simulation results. The thermodynamic parameters of 45# steel and Ni60PTA are obtained by JMatPro software, as shown in Fig. 1.

### 3.5 Finite element model

As described in Fig. 2, the dimensions of the substrate and cladding layer are 42 mm × 20 mm × 10 mm and 42 mm × 4 mm × 1 mm, respectively. The model is divided into transitional meshes. The grid division of the cladding layer is fine, and the grid of the substrate is sparse [24]. The selected element analysis type is coupled temperature–displacement, C3D8T.

In this study, a numerical simulation is conducted by varying the laser power and scanning speed. The laser power range is 1400–1600 W, and the scanning speed range is 3–5 mm/s. Table 2 shows the specific simulation scheme.

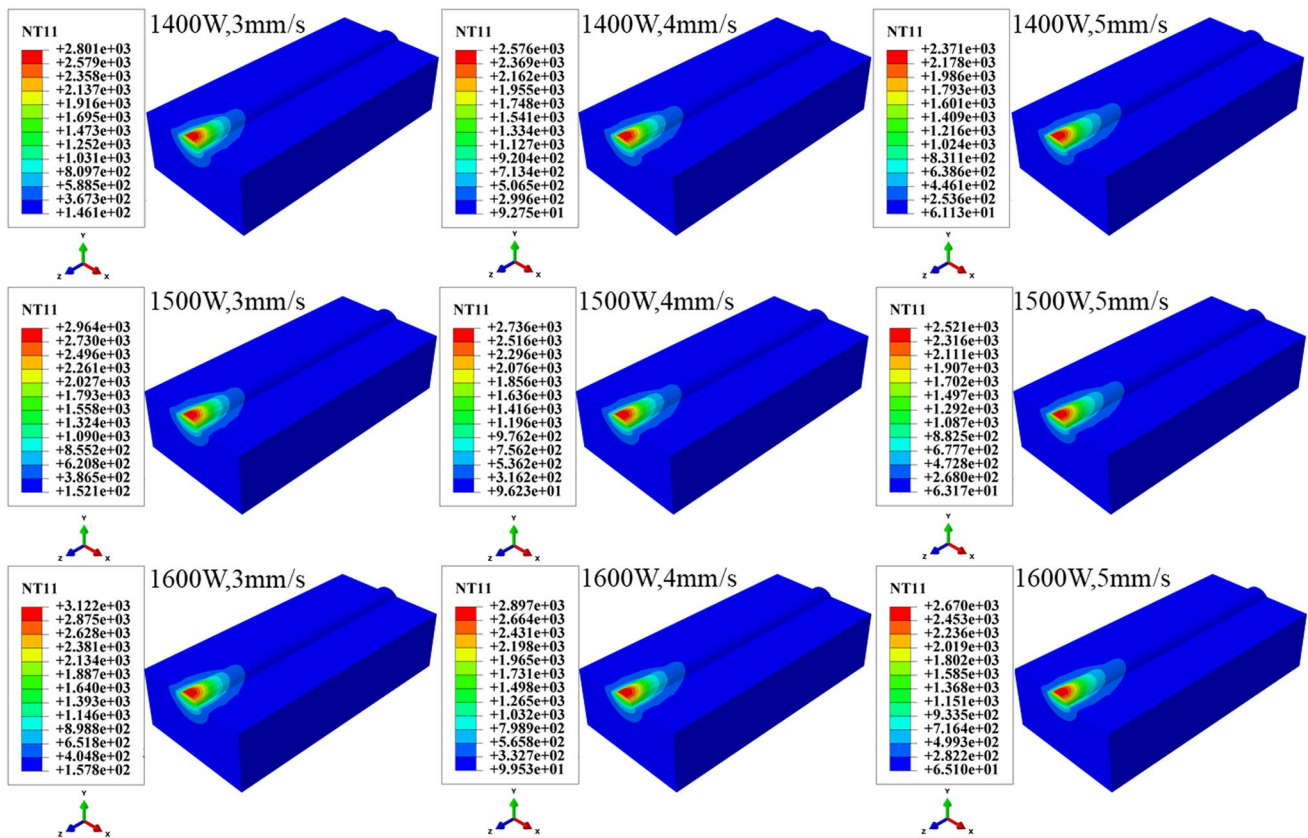


**Fig. 3** Temperature field results under different process parameters



## 4 Results and discussion

### 4.1 Optimal process parameters

Figure 3 displays the temperature fields at the same position for different process parameters. The laser power is proportional to the temperature, and the scanning speed is inversely proportional to the temperature. When the process parameters are a laser power of 1400 W and a scanning speed of 5 mm/s, the temperature reaches the minimum value (2371 °C). Figure 4 shows the microscopic morphology of the bonding zone with different process parameters. An obvious dividing line exists between the molten pool and the heat-affected zone under different process parameters, which proves that all nine groups of process parameters can form good metallurgical bonding [25]. Furthermore, the microstructure with laser power (1400 W) and scanning speed (5 mm/s) is finer than the others within the range of the selected process parameters. With the increase in scanning speed, the laser stays on the cladding layer for a shorter time, which results in less energy input to the molten pool per

unit time. Less energy is input into the molten pool per unit time, and the temperature gradient, cooling and solidification speed are relatively high. Therefore, the nucleation rate is higher than the grain growth rate, which leads to a finer primary phase. Moreover, the laser power determines the heating of the molten pool and the substrate. Smaller laser power increases the heat in the cladding layer, which results in a smaller temperature gradient; this condition is not conducive to the growth of dendrites [20].

Figure 5 shows the residual stress field after cooling at room temperature. The residual stress is the smallest when the laser power is 1400 W and the scanning speed is 5 mm/s. Figure 6 shows the cross-section morphology of samples with different process parameters. Under the condition of a constant scanning speed, the number of cracks and pores is fewer when the laser power is smaller. This phenomenon is mainly due to that a smaller power can reduce the input heat energy into the sample, which narrows the thermal influence range. At the same time, the influence of surrounding materials on the expansion of the coating area is reduced, which leads to a reduction in residual stress. Fewer cracks and pores are produced, and the scanning

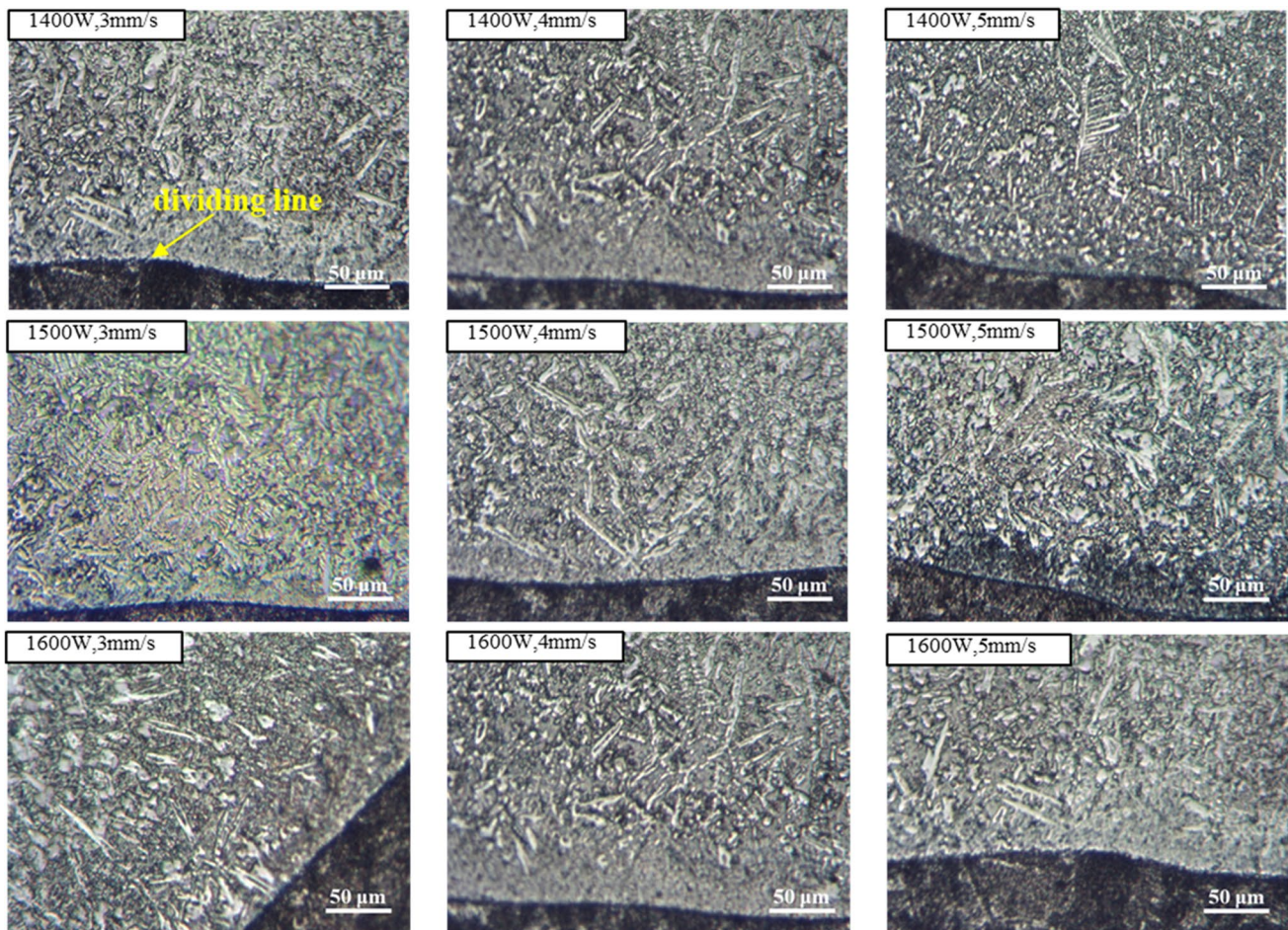


Fig. 4 OM morphologies of junctions under different process parameters

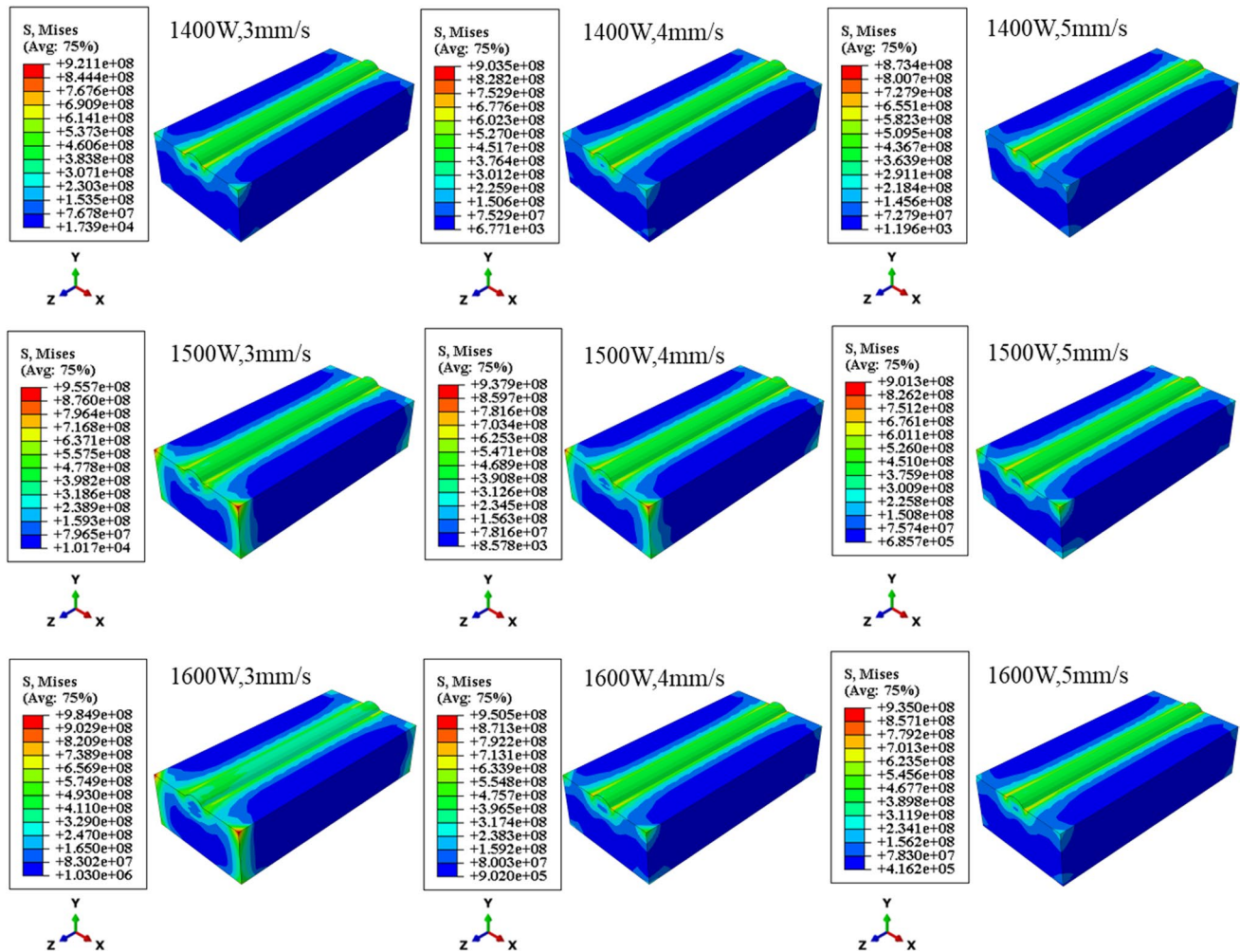


Fig. 5 Residual stress field results under different process parameters

speed is larger when the laser power is constant. The time of the laser beam acting on the cladding area is shortened with the increase in laser scanning speed. The effect of the nonmelting zone on the expansion and cooling solidification of the cladding zone is reduced. Therefore, the reduction in compressive residual stress weakens the tensile load capacity of the specimen and speeds up the crack growth rate [26]. In addition, no obvious cracks or pores are observed in the cross-section morphology of samples with a laser power of 1400 W and a scanning speed of 5 mm/s. By contrast, cracks or pores are found in other schemes.

Comparing the experimental and simulation results under nine sets of process parameters verifies that a laser power of 1400 W and a scanning speed of 5 mm/s are the optimal process parameters.

## 4.2 Temperature field analysis and verification

The joint between the coating and substrate along the X-axis is taken as Path 1, and the vertical direction from the coating

vertex to the substrate along the Y-axis direction is taken as Path 2. Some nodes are selected equidistantly in the radial and transverse directions. The specific paths and nodes are shown in Fig. 7.

Figure 8a shows the temperature changes at each point in the horizontal direction. The temperature of each point has a similar trend with time. When the laser irradiates the coating centre area, the temperature at each point firstly rises rapidly until it reaches a maximum value, then decreases sharply and, lastly, becomes stable. In comparison, the maximum value decreases in the order of  $A_1$ ,  $B_1$ ,  $C_1$ ,  $D_1$  and  $E_1$ . Figure 8b shows the temperature changes at each point in the radial direction. The temperature of the points in the radial direction increases first and then decreases with time, which is the same as that of the points in the horizontal direction. With the increasing distance in the depth direction, the maximum temperature of  $B_2$ – $E_2$  shows a gradual downwards trend.

The temperature distribution affects the solidification behaviour of the formed superalloy parts, and the



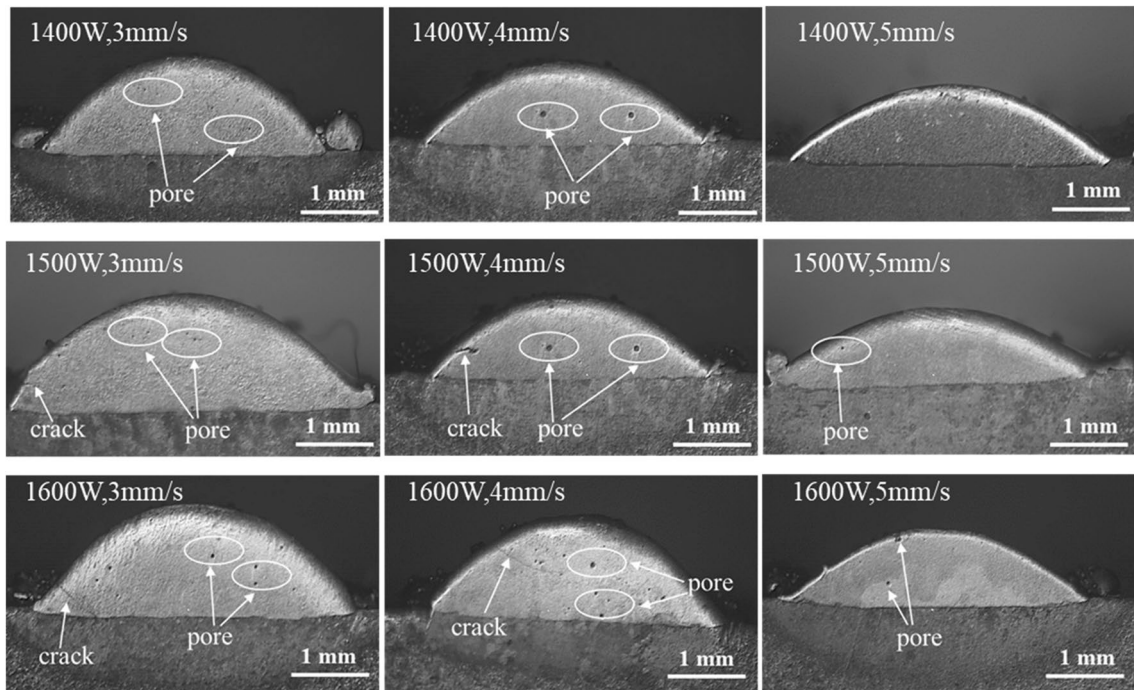


**Fig. 6** Cross-section OM morphologies under different process parameters

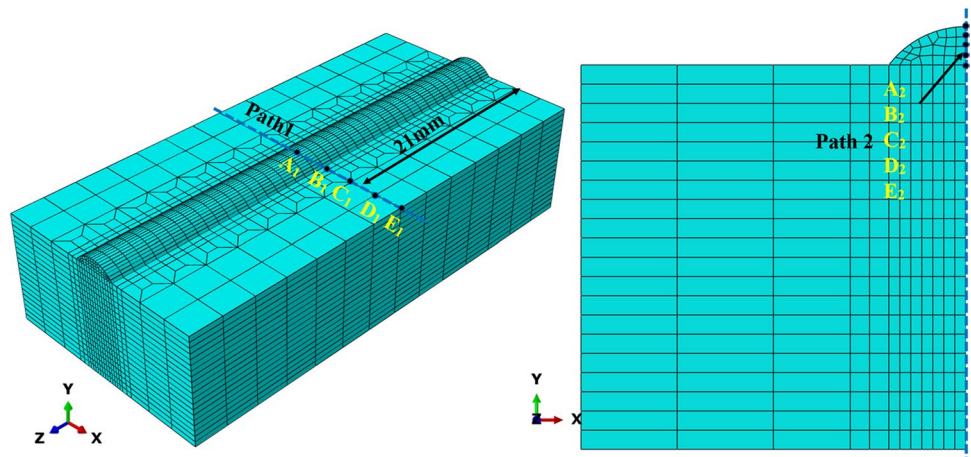
temperature gradient ( $G$ ) and solidification growth rate ( $S$ ) affect the solidification structure of the superalloy. The combined parameters of  $G$  and  $S$  and the cooling rate ( $G \times S$ ) affect the size of the microstructure, and the microscopic tissue size is finer when the cooling rate is larger. Morphological parameters ( $G/S$ ) affect the morphology of the microstructure. The morphology of the microstructure changes from equiaxed crystal to cellular crystal, columnar crystal and equiaxed crystal with the decrease in  $G/S$  [27].

The temperature at every moment can be fitted by a higher-order polynomial. Therefore, the solidification time, cooling rate, solidification rate and temperature gradient in

the direction of the coating depth can be calculated [11] according to Fig. 8b. Table 3 shows the corresponding calculation results. Figure 9 shows the cooling rate and solidification rate of the coating from bottom to top. The cooling rate increases instantly with the increase in solidification distance. At the top of the coating, the cooling rate reaches a maximum value of  $514\text{ }^\circ\text{C/s}$ . The solidification rate increases slowly when the solidification distance is from 0 to 0.25 mm. Then, the solidification rate increased rapidly from 25 to 125 mm/s.

According to Fig. 9 and Table 3, the microstructure evolution at different depths can be predicted and compared with

**Fig. 7** Schematic of paths and nodes



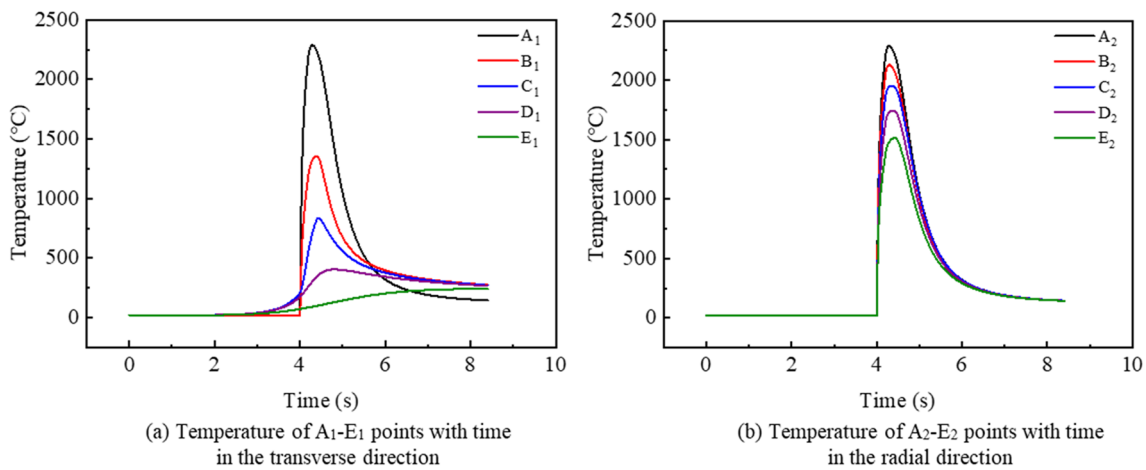


Fig. 8 Temperature variation of points in different directions

Table 3 Cooling rate, solidification rate and temperature gradient of nodes A<sub>2</sub>–E<sub>2</sub>

Node	Solidification distance (mm)	Solidification time (s)	Solidification rate (mm/s)	Cooling rate (°C/s)	Temperature gradient (°C/mm)
A <sub>2</sub>	1	4.178	125	514	633
B <sub>2</sub>	0.75	4.176	62.5	476	744
C <sub>2</sub>	0.5	4.172	25	432	814
D <sub>2</sub>	0.25	4.162	1.9	384	903
E <sub>2</sub>	0	4.143	1.6	331	1250

the experimental results. Figure 10 displays the cross section and the corresponding microstructure in different zones. Figure 10b–d correspond to the top, middle region and bottom regions of the coating, respectively. The top region has a very fine grain structure due to a higher cooling rate. In

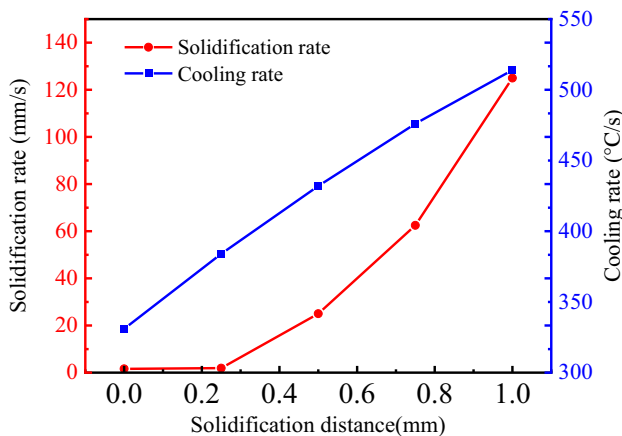


Fig. 9 Cooling rate and solidification rate from bottom to top of the coating

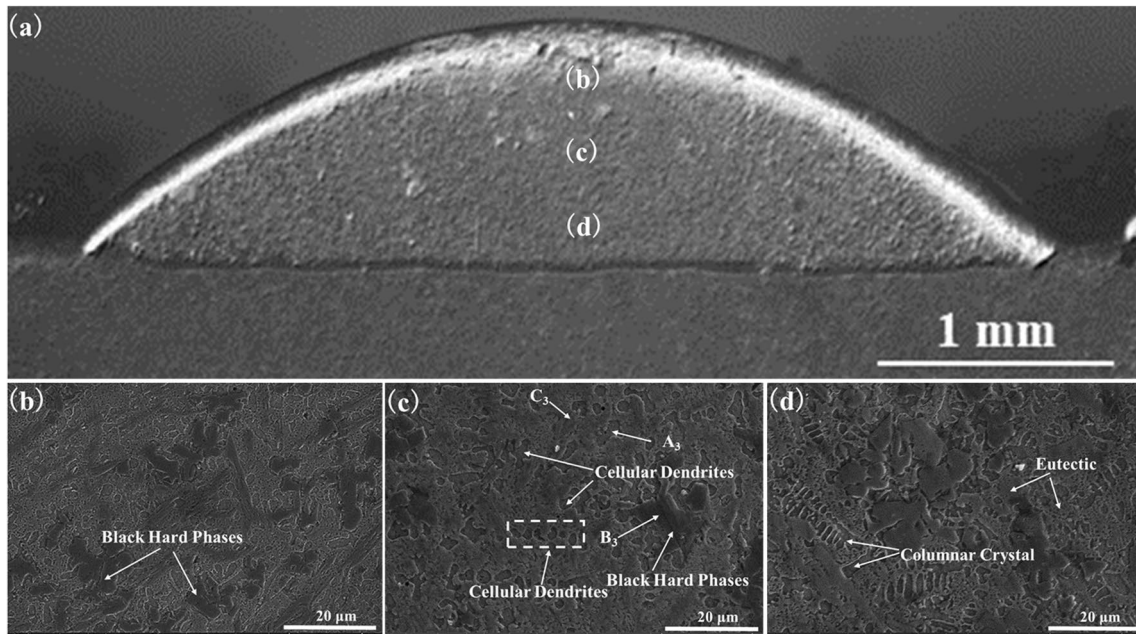
the middle region, cellular crystals and cellular dendrites are observed. The bottom region has a rough structure and columnar crystals. The reason is that the cooling rate ( $G \times S$ ) is lower and the morphology parameter ( $G/S$ ) is higher in the bottom region. The formation mechanism of the cladding layer microstructure is revealed through the combination of numerical simulation and experiment.

Figure 11 shows the temperature contours of local areas. Figure 11a displays that the outline of the molten pool presents an oval shape. The molten pool is in the shape of a spoon, as shown in Fig. 11b, on the longitudinal section along the laser cladding direction. Furthermore, the molten pool presents a comet-tail phenomenon. At the front end of the molten pool, the isotherm is dense, and the temperature gradient is large, whilst the isotherm is sparse and the temperature gradient is small at the back end. Figure 11c shows the comparison between the simulation and experimental results. The experimental and simulation results agree well with each other [28].

### 4.3 Stress field analysis and verification

The distribution characteristics of the residual stress field are shown in Fig. 12. The residual stress close to the substrate

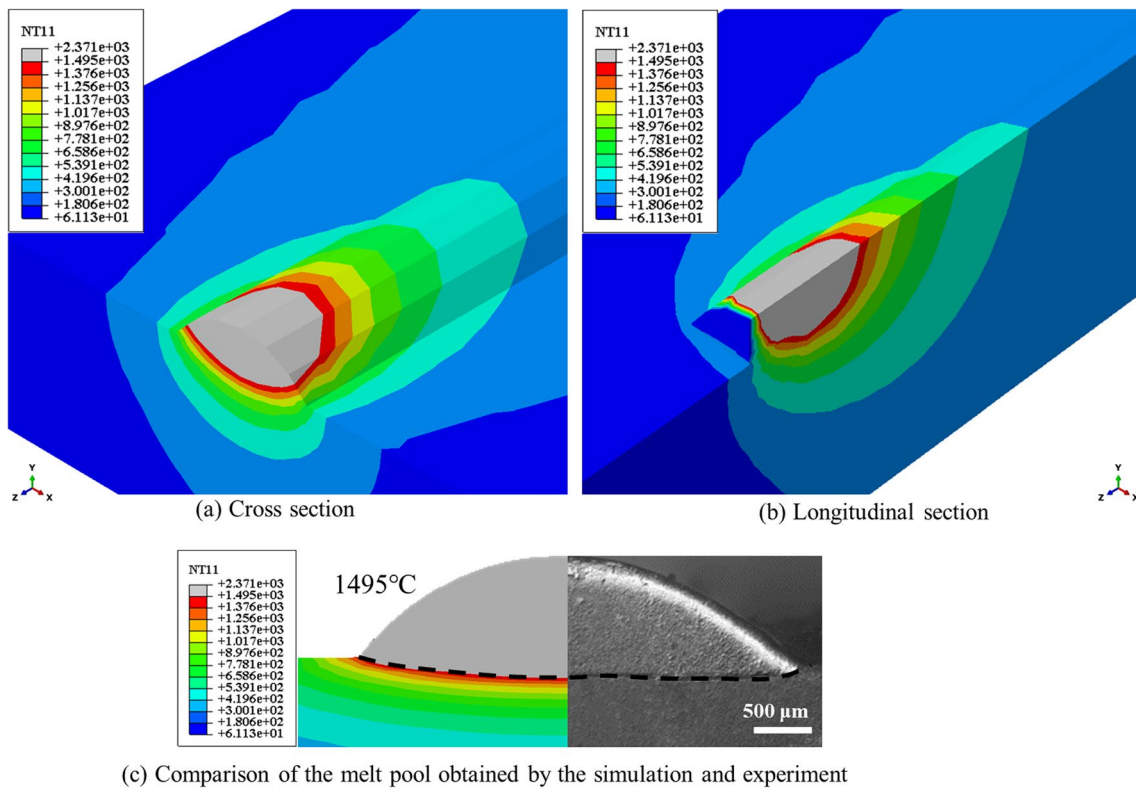




**Fig. 10** Morphology of the **a** cross section of the coating, **b** top region, **c** middle region and **d** bottom region

on both sides of the cladding layer is high, whether on the surface (Fig. 12a) or on the cross section (Fig. 12b). The material characteristics of the coating and substrate are

considerably different, especially in the thermal expansion coefficient. Thus, the residual stress on both sides of the cladding layer is relatively concentrated, and it is easy to



**(c)** Comparison of the melt pool obtained by the simulation and experiment

**Fig. 11** Temperature contours of local areas

**Fig. 12** Residual stress after cooling. **a** Surface residual stress and **b** cross-section residual stress

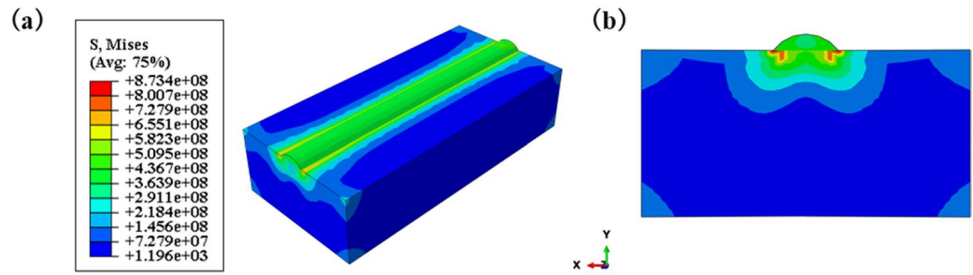


**Fig. 13** Partial enlarged view of the cross-section morphology of the sample with a laser power of 1500 W and a scanning speed of 3 mm/s

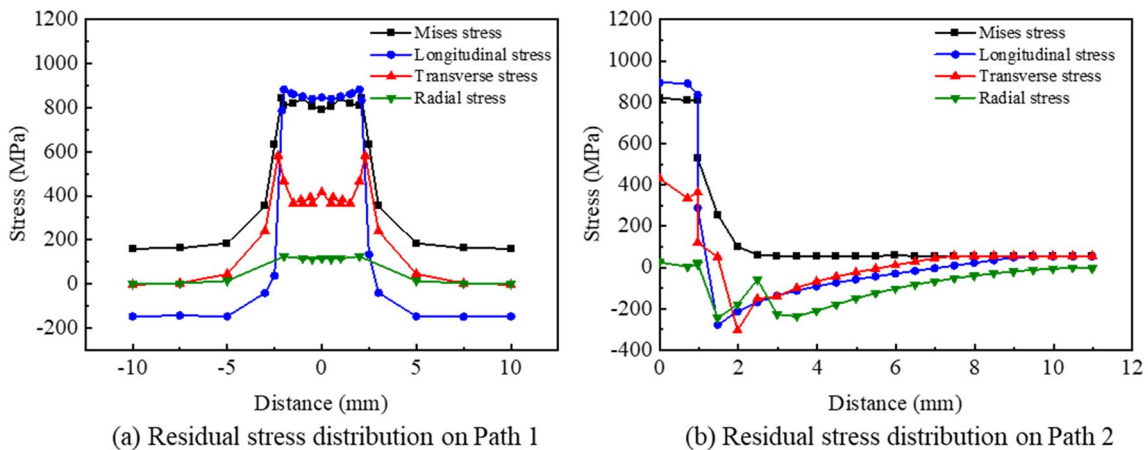
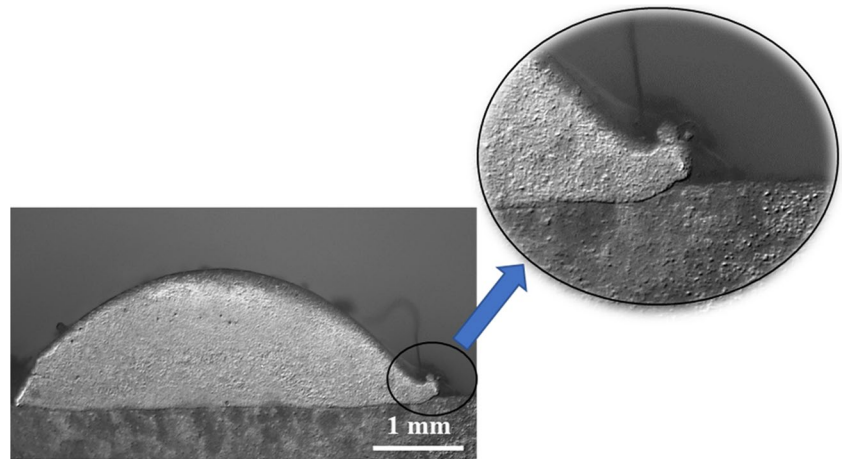


**Fig. 14** Residual stress distribution on two paths

crack. Figure 13 is a partially enlarged view of the cross-section morphology of the sample with a laser power of 1500 W and a scanning speed of 3 mm/s. Cracking occurs at the junction of the cladding layer and substrate, which verifies the accuracy of the simulation.

Figure 14a shows the trend of residual stress on Path 1 (refer to Fig. 7). The results show that the variation trend of residual stress is similar in all directions. The residual

stress increases sharply when approaching the boundary area of the coating, whilst it decreases in the coating. The reason is that the heat dissipation at the boundary between the coating and substrate is relatively fast, the temperature gradient increases and the stress value rises. On the contrary, the temperature gradient in the area near the centre of the spot inside the coating is small, which results in a low stress value. The von Mises stress on Path 1 shows tensile



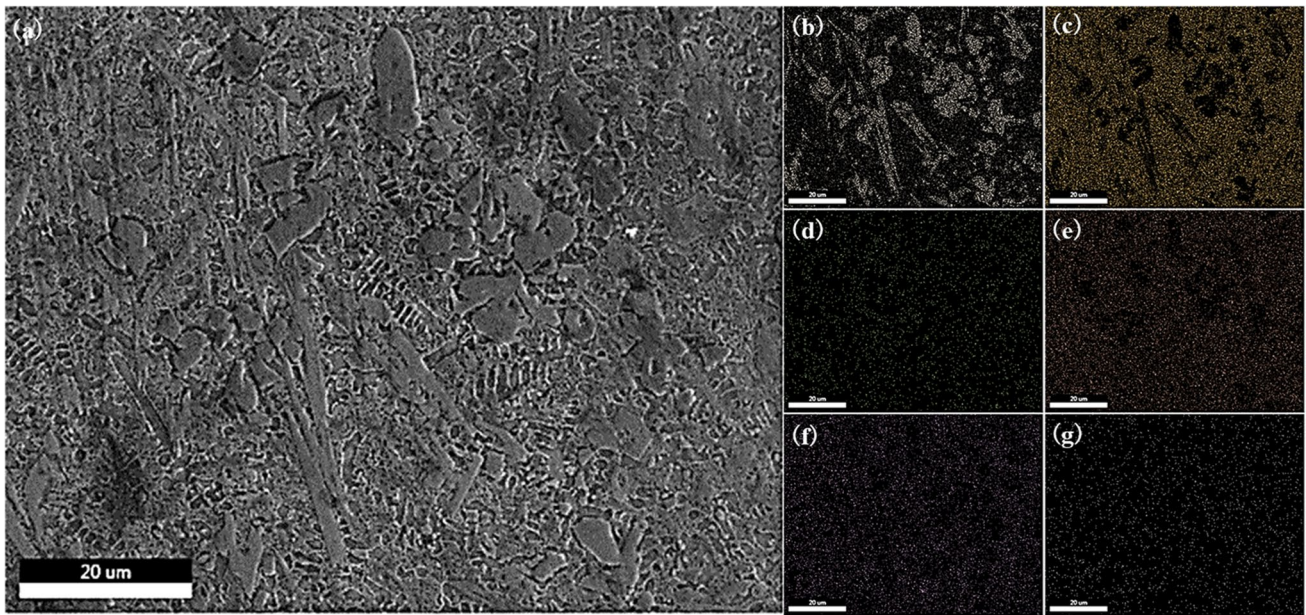


**Fig. 15** EDS mapping results. **a** Selected regions, **b** Cr, **c** Ni, **d** C, **e** Fe, **f** Si and **g** B

stress, and the maximum stress can reach 845 MPa. Longitudinally, the maximum tensile stress near the coating reaches 862 MPa, whilst the compressive stress appears far from the coating. This phenomenon is related to the shrinkage of 45# steel being less than that of the Ni-based coating. After the sample is cooled, the substrate prevents shrinkage of the Ni-based coating, which results in compressive stress. The deformation and stress in the transverse direction are relatively small due to the limited coating width. For the radial direction, the overall tensile stress appears, but the stress value is far less than that in other directions.

Figure 14b shows the residual stress trend on Path 2. The distribution of residual stress in all directions decreases

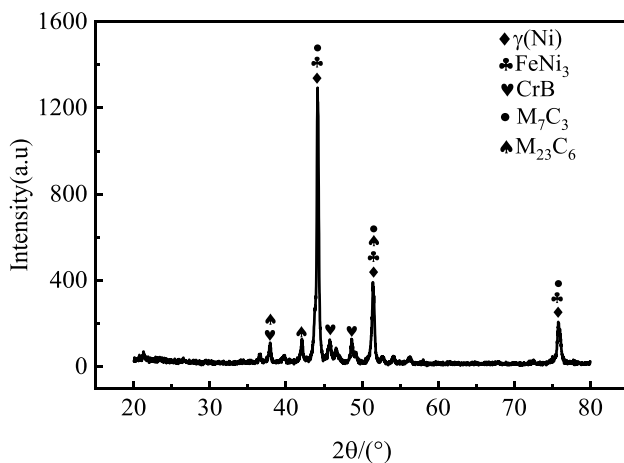


**Fig. 16** XRD pattern of the Ni60PTA laser cladding layer

gradually, and a large residual tensile stress is observed in the coating and its adjacent area. The longitudinal residual stress is high, whilst the transverse and radial residual stresses are relatively small. This stress distribution is consistent with that on Path 1. The tensile stress of the cladding layer and the compressive stress of the heat-affected zone are balanced due to the interaction of stress. Therefore, some residual compressive stress is found near the heat-affected zone.

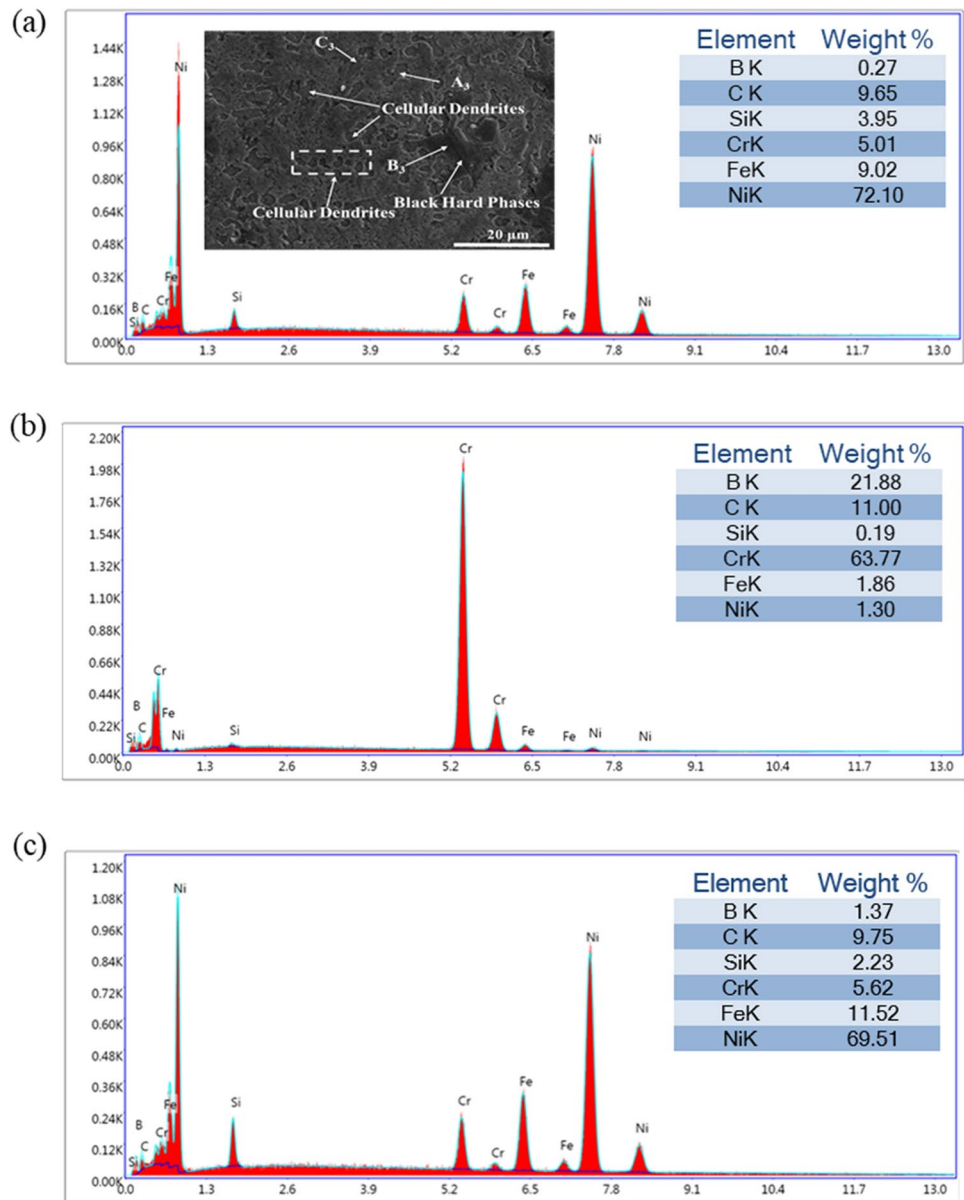
#### 4.4 Microstructures of coatings

Figure 15 shows the distribution of Cr, Ni, C, Fe, Si, and B in the coating. The EDS mapping results reveal that the structure is rich in Cr, and the brighter structures are rich in Ni and Fe.

Figure 16 shows the XRD spectrum of the coating. The phases in the coating are  $\gamma$ -(Ni),  $\text{FeNi}_3$ , M (M = Fe, Ni, Cr) $_{23}\text{C}_6$ ,  $\text{M}_7\text{C}_3$  and CrB. The EDS analysis of the points identified is presented in Fig. 17. The XRD analysis shows that the amount of Ni in cellular dendrite  $\text{A}_3$  is 72.10 wt%, and small amounts of Fe, Si, B and C are found. The cellular dendrites can be inferred to be  $\gamma$ -(Ni) solid solutions. The amounts of Cr and B in the black hard phase at  $\text{B}_3$  are high, and certain amounts of Fe, Ni and C are observed. Therefore, the black hard phase can be inferred to be  $\text{M}_{23}\text{C}_6$ ,  $\text{M}_7\text{C}_3$  and CrB. In the eutectic structure  $\text{C}_3$ , the amount of Ni is 69.51 wt%, and small amounts of Si, Fe and B are detected, which are in a continuous network structure and fill in the precipitated



**Fig. 17** EDS analysis of the coating. **a** A<sub>3</sub>, **b** B<sub>3</sub> and **c** C<sub>3</sub>



phase and  $\gamma$ -(Ni) in the gap around the solid solution. The results in [29] indicate that these structures are eutectic structures of Ni–B–Si.

#### 4.5 Microhardness distribution

Figure 18 shows the microhardness of the Ni-based coating. The hardness change shows a downwards trend. Alloy elements dissolve in the Ni-based solid solution at a high speed due to the convection of gas and liquid in the molten pool. This phenomenon forms a fairly stable Ni-based supersaturated solid solution, which has an obvious solid solution-strengthening effect. At the same time, Cr, Ni and Fe

interact with the substrate or other elements to form  $\text{FeNi}_3$ ,  $\text{M}$  ( $\text{M} = \text{Fe}, \text{Ni}, \text{Cr}$ ) $_{23}\text{C}_6$ ,  $\text{M}_7\text{C}_3$  and  $\text{CrB}$ , which have dispersion-strengthening effects. The combined effect of solid solution strengthening and dispersion strengthening greatly improves the hardness. The heat-affected zone absorbs a large amount of heat under the action of the molten pool. At the same time, the substrate melts slightly and then cools rapidly, which is equivalent to secondary quenching. The surface of the substrate is transformed, ferrite and pearlite are partially transformed into martensite [30] and the hardness of the heat-affected zone is higher than that of the substrate. The results show that the microhardness of the coating ( $600 \text{ HV}_{0.2}$ ) is approximately three times that of 45# steel ( $200 \text{ HV}_{0.2}$ ).

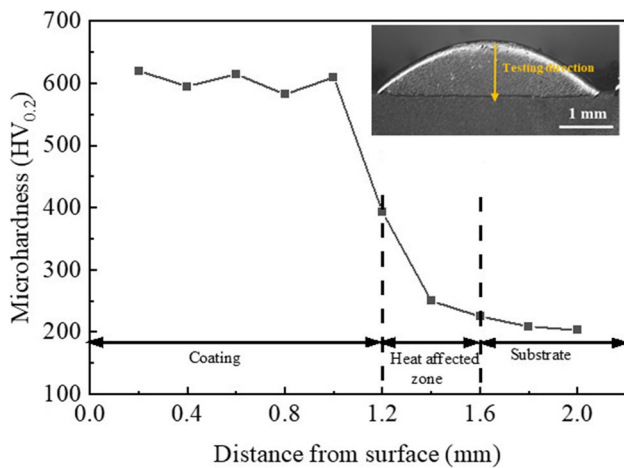


Fig. 18 Microhardness of the Ni-based coating

## 5 Conclusions

The finite element model of the Ni-based (Ni60PTA) cladding layer was established by ABAQUS software. From the analysis of the numerical simulation and experimental results, the following conclusions can be obtained:

- (1) The optimal process parameters are a laser power of 1400 W and a scanning speed of 5 mm/s. These parameters result in good morphology and can form an excellent metallurgical bond. The microstructure of the cladding layer is mainly  $\gamma(\text{Ni})$ ,  $\text{FeNi}_3$ ,  $\text{M}$  ( $\text{M} = \text{Fe}, \text{Ni}, \text{Cr}$ ) $_{23}\text{C}_6$ ,  $\text{M}_7\text{C}_3$  and CrB. The average microhardness of the cladding layer is 600 HV<sub>0.2</sub>, which is approximately three times that of 45# steel.
- (2) Horizontally, the maximum temperature at point  $A_1$  is 2371 °C, and the maximum temperature time points of  $B_1$ ,  $C_1$ ,  $D_1$  and  $E_1$  are delayed in sequence. Longitudinally, the temperature of each node reaches the peak at the same time. The maximum temperature of points  $A_2$ – $E_2$  decreases gradually with the increase in the distance in the depth direction.
- (3) The cooling rate at the top of the cladding is fast with a value of 667 °C/s, and this region has a very fine grain structure. The cooling rate at the middle is slow with a value of 552 °C/s, and this region transforms the cellular crystals into cellular dendrites. The cooling rate at the bottom further slows down to 305 °C/s. Thus, the structure in this region is relatively coarse.
- (4) The simulation results of the residual stress of the coating show that the residual stress is concentrated at the edges of both sides of the cladding layer and near the bonding bone. On Path 1, the residual tensile stress near the boundary of the cladding increases sharply

to 845 MPa. On Path 2, the maximum residual stress is 862 MPa, and the stress in all directions gradually decreases.

**Author contribution** Haiyang Long: writing—original draft, project administration, conceptualization, review and editing, investigation; Tiankai Li: review and editing, investigation, experimental; Zhen Dong: review and editing, investigation; Changming Qiu: experimental, conceptualization; Yongliang Gui: experimental, review and editing. Mingming Wang: investigation, review and editing. Dongdong Li: conceptualization, review and editing.

**Funding** This work is supported by the Science Fund for Distinguished Young Scholars of Hebei Province (E2019209473); this work is also supported by the Program for Top 100 Innovative Talents in Colleges and Universities of Hebei Province (SLRC2019030).

## Declarations

**Ethics approval** The authors claim that there are no ethical issues involved in this research.

**Consent to participate** All the authors consent to participate in this research and contribute to the research.

**Consent for publication** All the authors consent to publish the research. There are no potential copyright/plagiarism issues involved in this research.

**Conflict of interest** The authors declare no competing interests.

## References

1. Chen W, Yang X, Li X, Chai C, Liu W (2022) Study on microstructure and properties of nickel-based self-lubricating coating by laser cladding. *Coatings* 12:753
2. Li X, Wang R, Xin Z, Dong Y, Xu J, Wei D (2021) Changes in surface roughness and microstructure of 45# steel after irradiation by electron beam. *Mater Lett* 296:129934
3. Zhang Z, Kovacevic R (2019) A thermo-mechanical model for simulating the temperature and stress distribution during laser cladding process. *Int J Adv Manuf Tech* 102:457–472
4. Wang X, Keya T, Chou K (2016) Build height effect on the Inconel 718 parts fabricated by selective laser melting. *Procedia Manuf* 5:1006–1017
5. Zhu L, Xue P, Lan Q, Meng G, Ren Y, Yang Z, Xu P, Liu Z (2021) Recent research and development status of laser cladding: a review. *Opt Laser Technol* 138:106915
6. Siddiqui AA, Dubey AK (2020) Recent trends in laser cladding and surface alloying. *Opt Laser Technol* 134:106619
7. Mahmood MA, Popescu A, Hapenciu C, Ristoscu C, Mihailescu IN (2020) Estimation of clad geometry and corresponding residual stress distribution in laser melting deposition: analytical modelling and experimental correlations. *Int J Adv Manuf Tech* 111:77–91
8. Šarga P, Brezinová J, Viňáš J, Pástor M, Brezina J (2022) Impact of cladding technology on residual stresses within the renovation of high pressure die casting molds. *Metals* 12:388
9. Wang D, Hu Q, Zeng X (2015) Residual stress and cracking behaviors of Cr13Ni5Si2 based composite coatings prepared by laser-induction hybrid cladding. *Surf Coat Technol* 274:51–59

10. Yong Y, Fu W, Deng Q, Chen D (2017) A comparative study of vision detection and numerical simulation for laser cladding of nickel-based alloy. *J Manuf Process* 28(2):364–372
11. Gao W, Zhao S, Wang Y, Zhang Z, Liu F, Lin X (2016) Numerical simulation of thermal field and Fe-based coating doped Ti. *Int J Heat Mass Tran* 92:83–90
12. Zhang Q, Xu P, Zha G, Ouyang Z, He D (2021) Numerical simulations of temperature and stress field of Fe-Mn-Si-Cr-Ni shape memory alloy coating synthesized by laser cladding. *Optik* 242:167079
13. Vundru C, Paula S, Singha R, Yanb W (2018) Numerical analysis of multi-layered laser cladding for die repair applications to determine residual stresses and hardness. *Adv Manuf* 26:952–961
14. Ahn J, He E, Chen L, Pirling T, Dear JP, Davies CM (2018) Determination of residual stresses in fibre laser welded AA2024-T3 T-joints by numerical simulation and neutron diffraction. *Mat Sci Eng A-Struct* 712:685–703
15. Akbari M, Saedodin S, Toghraie D, Shoja-Razavi R, Kowsari F (2014) Experimental and numerical investigation of temperature distribution and molten pool geometry during pulsed laser welding of Ti6Al4V alloy. *Opt Laser Technol* 59:52–59
16. Liu Y, Zhang J, Pang Z (2018) Numerical and experimental investigation into the subsequent thermal cycling during selective laser melting of multi-layer 316L stainless steel. *Opt Laser Technol* 98:23–32
17. Wu J, Wang L, An X (2017) Numerical analysis of residual stress evolution of AlSi10Mg manufactured by selective laser melting. *Optik* 137:65–78
18. Gan Z, Gang Y, He X, Li S (2017) Numerical simulation of thermal behavior and multicomponent mass transfer in direct laser deposition of Co-base alloy on steel. *Int J Heat Mass Tran* 104:28–38
19. Gan Y, Wang W, Cui Z, Yan X, Guan Z, Xu B (2015) Numerical and experimental study of the temperature field evolution of Mg alloy during high power diode laser surface melting. *Optik* 126(7–8):739–743
20. Liu H, Li M, Qin X, Huang S, Hong F (2019) Numerical simulation and experimental analysis of wide-beam laser cladding. *Int J Adv Manuf Tech* 100(1):237–249
21. Liu H, Qin X, Wu M, Ni M, Huang S (2019) Numerical simulation of thermal and stress field of single track cladding in wide-beam laser cladding. *Int J Adv Manuf Tech* 104:3959–3976
22. Lv H, Liu Y, Chen H, Zhang W, Lv S, He D (2023) Temperature field simulation and microstructure evolution of Fe-based coating processed by extreme high-speed laser cladding for re-manufacturing locomotive axle. *Surf Coat Technol* 464:129529
23. Gao J, Wu C, Hao Y, Xu X, Guo L (2020) Numerical simulation and experimental investigation on three-dimensional modelling of single-track geometry and temperature evolution by laser cladding. *Opt Laser Technol* 129:106287
24. Gao W, Zhao S, Wang Y, Liu F, Zhou C, Lin X (2014) Effect of re-melting on the cladding coating of Fe-based composite powder. *Mater Design* 64:490–496
25. Gao W, Chang C, Li G, Xue Y, Wang J, Zhang Z, Lin X (2019) Study on the laser cladding of FeCrNi coating. *Optik* 178:950–957
26. Song M, Wu L, Liu J, Hu Y (2021) Effects of laser cladding on crack resistance improvement for aluminum alloy used in aircraft skin. *Opt Laser Technol* 133:106531
27. Li C, Yu Z, Gao J, Zhao J, Han X (2018) Numerical simulation and experimental study of cladding Fe60 on an ASTM 1045 substrate by laser cladding. *Surf Coat Technol* 357:965–977
28. Zhang T, Zhang Q, Yao B, Li B (2021) Numerical simulation of temperature field and stress field of Ni-based laser cladding layer on TC4 surface. *Laser Optoelectron Prog* 58(3):220–228
29. Wang W, Liu L, Zhang X, Shi Z, Tian Y, Lin J (2020) Microstructures and mechanical properties of Ni60 alloy fabricated by laser metal deposition. *Mater Res Express* 7(1):016569
30. Wu Z, Li T, Li Q, Shi B, Zhang HC (2019) Process optimization of laser cladding Ni60A alloy coating in remanufacturing. *Opt Laser Technol* 120:105718

**Publisher's Note** Springer Nature remains neutral with regard to jurisdictional claims in published maps and institutional affiliations.

Springer Nature or its licensor (e.g. a society or other partner) holds exclusive rights to this article under a publishing agreement with the author(s) or other rightsholder(s); author self-archiving of the accepted manuscript version of this article is solely governed by the terms of such publishing agreement and applicable law.